






# On the Reliability of Photometric and Spectroscopic Tracers of Halo Relaxation

Mohammad H. Zhooldideh Haghghi<sup>1</sup> , Mojtaba Raouf<sup>1,2</sup> , Habib. G. Khosroshahi<sup>1</sup>, Amin Farhang<sup>1</sup> , and Ghassem Gozaliasl<sup>3</sup>

<sup>1</sup>School of Astronomy, Institute for Research in Fundamental Sciences (IPM), Tehran, 19395–5746, Iran; [mzhooldideh@ipm.ir](mailto:mzhooldideh@ipm.ir)

<sup>2</sup>Korea Astronomy and Space Science Institute, 776 Daedeokdae-ro, Yuseong-gu, Daejeon 305-348, Republic of Korea

<sup>3</sup>Department of Physics, University of Helsinki, P.O. Box 64, FI-00014, Helsinki, Finland

Received 2020 May 11; revised 2020 September 25; accepted 2020 September 28; published 2020 November 19

## Abstract

We characterize the relaxation state of galaxy systems by providing an assessment of the reliability of the photometric and spectroscopic probe via the semianalytic galaxy evolution model. We quantify the correlations between the dynamical age of simulated galaxy groups and popular proxies of halo relaxation in observation, which are mainly either spectroscopic or photometric. We find the photometric indicators demonstrate a stronger correlation with the dynamical relaxation of galaxy groups compared to the spectroscopic probes. We take advantage of the Anderson Darling statistic ( $A^2$ ) and the velocity segregation ( $\Delta V$ ) as our spectroscopic indicators, and use the luminosity gap ( $\Delta m_{12}$ ) and the luminosity decentering ( $D_{\text{offset}}$ ) as photometric ones. First, we find that a combination of  $\Delta m_{12}$  and  $D_{\text{offset}}$  evaluated by a bivariate relation ( $B = 0.04 \times \Delta m_{12} - 0.11 \times \text{Log}(D_{\text{offset}}) + 0.28$ ) shows a good correlation with the dynamical age compared to all other indicators. Second, by using the observational X-ray surface brightness map, we show that the bivariate relation brings about some acceptable correlations with X-ray proxies. These correlations are as well as the correlations between  $A^2$  and X-ray proxies, offering a reliable yet fast and economical method of quantifying the relaxation of galaxy systems. This study demonstrates that using photometric data to determine the relaxation status of a group will lead to some promising results that are comparable with the more expensive spectroscopic counterpart.

*Unified Astronomy Thesaurus concepts:* [Galaxy clusters \(584\)](#); [Galactic and extragalactic astronomy \(563\)](#); [Galaxy groups \(597\)](#); [Sloan photometry \(1465\)](#); [N-body simulations \(1083\)](#)

## 1. Introduction

Observations have revealed that galaxy environments such as groups and clusters influence the properties of the member galaxies (Hashimoto et al. 1998; Hou et al. 2013). Nearly half of the galaxy population inhabits in groups (Eke et al. 2005). They depute an intermediate-mass regime in which a significant population of both spirals and ellipticals are observed (McGee et al. 2011). In the hierarchical structure formation paradigm, groups are progenitors of galaxy clusters; thus, their role in galaxies evolution is more significant than it appears (Ellison et al. 2008; Peng et al. 2015). For example, galaxy interaction and merger in a group environment can be more efficient because of a lower galaxy velocity compared to the same in a cluster environment, which would influence the morphology of galaxies (Barnes 1989), as well as their star formation (Wilman et al. 2005). It has been shown that galaxies in dynamically relaxed groups tend to be redder than galaxies in unrelaxed groups (Carollo et al. 2013; Raouf et al. 2019) and can grow, through mergers, to become giant galaxies that are mostly found in massive galaxy clusters (Khosroshahi et al. 2006).

Dynamically relaxed groups and clusters display a symmetric X-ray surface brightness distribution (Parekh et al. 2015), and they often have the brightest central galaxy that is located close to the peak of the X-ray emission, e.g., the bottom of the potential well (Khosroshahi et al. 2004; Skibba et al. 2011). The velocity distribution of member galaxies in a relaxed group is also expected to be Gaussian (Hou et al. 2009). On the other hand, unrelaxed or evolving galaxy groups and clusters are being formed and have been undergoing mergers.

Recent studies have highlighted the importance of the dynamical state of group-size halos in the observed properties

of galaxies. For instance, active galactic nucleus activities of luminous elliptical galaxies probed by their radio emission are shown to be correlated with the dynamical state of the parent halo (Khosroshahi et al. 2017). The brightest group galaxies (BGGs) in the late-formed groups are an order of magnitude more luminous in radio than their counterparts in early-formed groups, which is also confirmed by numerical simulations (Raouf et al. 2018). This follows several observational and numerical studies suggesting that the impact of the group environment on galaxies goes beyond simple overdensity indicators. Therefore, the dynamical state of a galaxy group and its relaxation state plays some role in galaxy evolution.

Fossil galaxy groups are arguably the extreme case of the dynamical relaxation in which luminous galaxies in groups merge to form a giant elliptical galaxy with the halo X-ray emission remaining as the fossil record of such an internal evolution (Ponman et al. 1994; Jones et al. 2003; Khosroshahi et al. 2006, 2007). The  $N$ -body cosmological simulations support this argument (D’Onghia et al. 2005; Dariush et al. 2007; Raouf et al. 2014). With the advances in the imaging surveys, many current and future large imaging surveys will benefit from reliable and economical methods of assigning *the age dating galaxy groups* introduced by Raouf et al. (2014). In the following studies, Lavoie et al. (2016), Horellou et al. (2018), and Gozaliasl et al. (2019) used the luminosity gap between two most luminous galaxies in the group,  $\Delta m_{12}$ , and/or the offset between the brightest group galaxies and the luminosity centroid,  $D_{\text{offset}}$ , to probe the relaxation and dynamical age of halos.

There are several approaches for parameterizing halo relaxation. If the X-ray data are available, the photon asymmetry (Nurgaliev et al. 2013) or centroid shift (Böhringer

et al. 2010) can be used as indicators. In the case of photometric data, the indicators are generally the luminosity gap (Jones et al. 2003) and the BGG offset (Sanderson et al. 2009). Also, some spectroscopic indicators could be used, such as velocity segregation (Lares et al. 2004; Nascimento et al. 2019; Raouf et al. 2019) and the Anderson Darling (AD) test that is based on the Gaussianity of the velocity distribution (Hou et al. 2009) of group galaxies. It is worth mentioning that since X-ray observations are both more expensive and less available than spectroscopic or photometric observations, some suggest that it would be better to use the AD test instead of X-ray probes (Roberts et al. 2018). They come to this conclusion by investigating the correlation between X-ray indicators and the AD test and showing that these quantities correlate strongly.

In this study, we investigate the reliability of photometric, spectroscopic, and X-ray proxies to determine the dynamical state of galaxy groups. In the era of large surveys, a reliable and yet economical method of characterizing the halo dynamical state would be of great advantage for statistical studies aimed at understanding *the role of environment on galaxy properties*. Motivated by our previous studies employing the luminosity gap and the BGG offset, we introduce a bivariate correlation that is a combination of  $\Delta m_{12}$  and  $D_{\text{offset}}$  to test whether we can overcome the superiority of the AD test,  $A^2$ , which is explored by Hou et al. (2009, 2013). In our study, we use galaxies drawn from the semianalytic models of Raouf et al. (2017), based on the Millennium Simulation (Springel et al. 2005), the so-called Radio–Semi-Analytic Galaxy Evolution (SAGE). The advantage of simulated data is that through the semianalytic models we can reliably obtain the mass assembly history of a dark matter halo. We also apply our finding on observed galaxy groups of the Yang catalog (Yang et al. 2005, 2007) to compare the predictions of the simulations with the observations. Throughout this paper, we adopt  $H_0 = 100h \text{ km s}^{-1} \text{ Mpc}^{-1}$  for the Hubble constant with  $h = 0.73$ .

## 2. Data and Mock Catalog

### 2.1. Simulated Data

In this study we use the public release of the Millennium Simulation with a  $\Lambda$ CDM cosmology and the following parameters:  $\Omega_m = 0.25$ ,  $\Omega_b = 0.045$ ,  $\Omega_\Lambda = 0.75$ ,  $h = 0.73$ , and  $n = 1, \sigma_8 = 0.9$ . The simulation box ( $500h^{-1} \text{ Mpc}$ )<sup>3</sup> contains  $2160^3$  particles and presents the mass resolution of  $8.6 \times 10^8 h^{-1} M_\odot$ . The dark matter merger trees within each simulation snapshot (64 snapshots) are expanded approximately logarithmically in time between  $z = 127$  and  $z = 0$  and extracted from the simulation using a combination of friend-of-friend (FoF; Davis et al. 1985) and SUBFIND (Springel et al. 2001) halo finders algorithm. The gas and stellar components of galaxies in dark matter halos are constructed semianalytically, based on different phenomenological recipes. We are using the radio semianalytic galaxy evolution (Raouf et al. 2017, Radio–SAGE) galaxy formation model that self-consistently follows the gas cooling–heating cycle in different types of galaxies and is calibrated to match key observations for various redshifts (Raouf et al. 2019). The galaxy catalog contains  $\sim 51,000$  halos with masses above  $10^{13} h^{-1} M_\odot$  and  $\sim 5$  million galaxies from which we only select galaxies brighter than  $-14$  in the  $r$ -band absolute magnitude for

completeness. Also, we have chosen systems with  $Mr_{\text{BGG}} < -21.5$  to remove the modest galaxies with dwarf satellites.

### 2.2. Mock Redshift–Space Catalog

To take into account the basic observational limitations, a mock catalog has been constructed from the algorithm described in Blaizot et al. (2005) without box transformations or replication. To do so we (i) place the observer at one of the vertices of the simulation box and look at the galaxies in the box through the observer lines of sight; (ii) then convert the Cartesian coordinate system (i.e.,  $X$ ,  $Y$ , and  $Z$ ) to celestial coordinates (i.e., R.A. and decl.); (iii) measure the redshift of each galaxy using the Duarte & Mamon (2015) algorithm; (iv) estimate the luminosity distance  $D_L$  of each galaxy, using their computed redshift and comoving distance; and (v) compute the apparent magnitude of each galaxy from  $D_L$  and the absolute magnitude. We estimate the uncertainties on the mean of our measurements in the same way that is described in Section 4.1 of Farhang et al. (2017). Finally, having the redshift of the objects, we can easily calculate the line-of-sight velocity of group members.

### 2.3. Observational Data

To have a fair comparison with the findings of Roberts et al. (2018), we select the same sample and the same data that they adopt. Therefore, we use galaxy groups/clusters with halo masses  $M_{\text{halo}} > 10^{13}$  provided by the Yang catalog (Yang et al. 2005, 2007), which are recognized through the FoF algorithm (Huchra & Geller 1982; Press & Davis 1982). To compute the clustercentric radii we use galaxies’ redshift, the angular separation between the galaxy position and the luminosity-weighted center of the cluster, and then we normalize it to  $R_{500}$ , which is the radii where the inner average density is 500 times the critical density of the universe.

A subset of the Yang catalog comprising clusters with a minimum of 10 spec- $z$  members is chosen to ensure an accurate classification, using the velocity profile shape (Hou et al. 2009). To study the relation between optical and X-ray relaxation indicators, we use a sample of 58 clusters by Roberts et al. (2018), which are found after cross-matching the Yang catalog with the Chandra and XMM-Newton X-ray observation archives. Only X-ray observations with clean exposure times  $\geq 10$  ks have been chosen. For the Chandra images, observations were reprocessed, cleaned, and calibrated by CIAO version 4.9, and CALDB version 4.7.5. Also, LC –CLEAN with a  $3\sigma$  threshold is used to filter background flares. In addition, charge transfer inefficiency and time-dependent gain corrections are taken into account. Images are created in the 0.5–5 keV energy band. By using the WAVDETECT script, point sources are identified and then filled with local Poisson noise using DMFILTH. Blank sky background images are generated for each observation using the BLANKSKY and BLANKSKY IMAGE scripts. For XMM-Newton, data reduction observations are done by SAS, version 16.0.0. Calibrated event files are generated using the EMCHAIN script, and filtered event lists were generated using MOS-FILTER. Like the CIAO images, exposure-corrected images are created in the 0.5–5 keV band, and point sources are identified with the CHEESE script and thereafter filled with local Poisson noise using the CIAO script DMFILTH. For more details on the

X-ray data reduction, we refer the reader to Roberts et al. (2018).

### 3. Mass Assembly History and Halo Relaxation Proxies

#### 3.1. Mass Assembly History

We assign a dynamical age to each cluster by obtaining the halo mass ratio at  $z \sim 0.5$ , 1 to  $z \sim 0$ , which we specify with  $\alpha_{z,0} = M_{200}(z = 0.5,1)/M_{200}(z = 0)$ . We define fast-growth and slow-growth modes associated with  $\alpha_{0.5,0}$  and  $\alpha_{1,0}$ , respectively. Our intuition is based on the fact that there would be less available time for halos to grow from  $z = 0.5$  compared to those halos growing from  $z = 1$ . According to our definition (Dariush et al. 2007; Raouf et al. 2014), a group is dynamically unrelaxed if it reaches less than one-third of its final mass by  $z \sim 1$  ( $\alpha_{1,0} < 0.3$ ) and is relaxed if it reaches more than one-half of its total present-day mass by  $z \sim 1$  ( $\alpha_{1,0} > 0.5$ ). In our earlier studies (Raouf et al. 2016), we showed a sample of relaxed groups selected based on the luminosity gap and the BGG/brightest cluster galaxy (BCG) offset from the halo center will result in a contaminated sample with a high dynamical age ( $\alpha_{1,0} > 0.5$ ). Nevertheless, we note that this method for estimating the dynamical age is not unique and may show different results when we track the halo individually (e.g., see trace method and scatters in Dariush et al. 2010; Gozaliasl et al. 2014; Farhang et al. 2017).

#### 3.2. Tracers Based on the Luminosity Distribution

##### 3.2.1. Luminosity Gap

One of the most promising and successful halo age indicators is the luminosity gap ( $\Delta m_{12}$ ). It is the magnitude difference between the first and second brightest galaxy within half the virial radius of a group as introduced by Jones et al. (2003) when it is larger than 2 mag for conventional definition of the fossil galaxy groups (Ponman et al. 1994). Alternatively, some authors prefer to use the stellar mass ratio between the second-most-massive and most-massive galaxies in a given group (Roberts et al. 2018). For a relaxed system, if the luminosity gap is large, then the stellar mass ratio  $M_2/M_1$  should be small, while for younger groups  $M_2/M_1$  has not reduced enough and is not so small.

##### 3.2.2. Luminosity Decentering

The BGG is expected to be located at the center of the group's halos if the group is dynamically relaxed (Ponman et al. 1994; Smith 2005). We are using optical luminosity decentering,  $D_{\text{offset}}$ , as a tracer of the dynamical age of the galaxy groups. Merging systems are unrelaxed and have their BGG displaced from the center of the group halo. To find the position of the halo center, alternatively, one can use the X-ray peak and the mass centroid from the gravitational lensing observations (Oguri et al. 2010; Dietrich et al. 2012; Gozaliasl et al. 2019). Given that the lensing mass map and the X-ray emission peaks are not directly accessible through cosmological simulations, we rely on the luminosity-weighted centroid of galaxy groups that is also economically available in the optical observations.

We calculate luminosity-weighted/centroid by using  $X_L = \sum X_i L_i / L_i$ , where  $L_i$  is the  $r$ -band luminosity of the  $i$ th galaxy in a group and  $X_i$  is the projected coordinate of each galaxy.

#### 3.2.3. Bivariant Correlation (B)

In order to come up with a more appropriate photometric probe, we combine  $\Delta m_{12}$  and  $D_{\text{offset}}$  into a linear bivariant correlation (B) as

$$B = C \times \Delta m_{12} + D \times \text{Log}(D_{\text{off-set}}) + E. \quad (1)$$

This bivariant correlation is basically a mixture of both centroid shift and luminosity gap. By studying the relation of B with  $\alpha_{z,0}$  and minimizing the scatter between these two quantities, we can determine the constant coefficients ( $C$ ,  $D$ , and  $E$ ) of the above relation. Specifically, these constants can be found via the least-squares method, after which we calculate the correlation coefficient between  $\alpha_{z,0}$  and B.

#### 3.3. Dynamical Tracers

##### 3.3.1. Anderson Darling Test

Some studies (Yahil & Vidal 1977; Ribeiro et al. 2013) show that the line-of-sight velocity distribution of member galaxies within a relaxed group/cluster is almost normal; however, the unrelaxed groups display a larger deviation from the normal velocity distribution. We can measure the deviation of the velocity distribution from normality by using Kolmogorov,  $\chi^2$ , or Anderson Darling (AD) tests. Since the AD test has been shown to be more powerful and reliable than other tests in detecting departures from an underlying Gaussian distribution (see Hou et al. 2009 for details and uncertainties), we employ this test to measure *how* much a velocity distribution of member galaxies deviates from a normal distribution.

The AD test relies on calculating the distance between the cumulative distribution functions (CDFs) of a specific distribution and an ideal normal distribution. This distance can be measured in terms of  $A^2$  according to the following relation:

$$A^2 = -n - \frac{1}{n} \sum_{i=1}^n [2i - 1] [\ln \Phi(x_i) + \ln(1 - \Phi(x_{n+1-i}))], \quad (2)$$

where  $x_i < x < x_i + 1$  and  $\Phi(x_i)$  is the CDF of the hypothetical underlying distribution. Large values of this statistic ( $A^2$ ) correspond to larger deviations from normality. In the case of a Gaussian distribution, which is what we are considering here, we have

$$\Phi(x_i) = \frac{1}{2} \left( 1 + \text{erf} \left( \frac{x_i - \mu}{\sqrt{2} \sigma} \right) \right). \quad (3)$$

By calculating  $A^2$  for a distribution with an arbitrary significance and comparing it with critical values we can conclude if a distribution is normal or not (Stephens 1974).

##### 3.3.2. Velocity Segregation ( $\Delta \bar{V}$ )

Another spectroscopic indicator that is helpful in determining the relaxation state of the galaxy groups is the velocity segregation. We calculate the velocity segregation between the BGG and the  $i$ th spectroscopic member galaxy within half the virial radius, using the following relation:

$$\Delta \bar{V} = \frac{\sum_{i=1}^{n-1} |V_{\text{BGG}} - V_i|}{n - 1}, \quad (4)$$

where  $n$  is the number of galaxies in a group,  $V_{BGG}$  and  $V_i$  are the line-of-sight velocities of the BGG and  $i$ th galaxy, respectively. Motivated from the velocity profile of groups and clusters,  $\Delta V$  should be smaller for relaxed systems; in contrast, it should be large for dynamically unrelaxed ones (see Figure 11 of Raouf et al. 2019).

### 3.4. Intracluster Medium Tracers

#### 3.4.1. Photon Asymmetry ( $A_{\text{phot}}$ )

Photon asymmetry is one of the best model-independent and most robust techniques to measure the asymmetry of the X-ray profiles (Nurgaliev et al. 2013). This novel method quantifies the degree of axisymmetry of X-ray photon distributions around the X-ray peak; in other words, it demonstrates how uniform photons are placed in a  $2\pi$  radian range within an annulus encompassing the cluster center. For a detailed explanation regarding the photon asymmetry we refer the reader to Nurgaliev et al. (2013). We take advantage of the photon asymmetry calculated by Roberts et al. (2018) using the following equation:

$$A_{\text{phot}} = 100 \frac{\sum_{j=1}^{N_{\text{ann}}} C_j \hat{d}_{N_j, C_j}}{\sum_{j=1}^{N_{\text{ann}}} C_j}, \quad (5)$$

where  $N_{\text{ann}}$  is the total number of annuli,  $C_j$  is number of cluster counts above background within  $j$ th annulus, and  $\hat{d}_{N_j, C_j}$  is an estimated distance between the true photon distribution and the uniform distribution, given as follows:

$$\hat{d}_{N, C} = \frac{N}{C^2} \left( U_N^2 - \frac{1}{12} \right), \quad (6)$$

where  $N$  is the total number of counts within each annulus, and  $C$  is the number of counts intrinsic to the cluster. In addition,  $U_N^2$  is Watson's statistic (Watson 1961), which can be achieved by minimizing the following equation:

$$U_N^2(\phi_0) = \frac{1}{12N} + \sum_{i=0}^{N-1} \left( \frac{2i+1}{2N} - F(\phi_i) \right)^2 - N \times \left( \frac{1}{2} - \frac{1}{N} \sum_{i=0}^{N-1} F(\phi_i) \right)^2, \quad (7)$$

here  $\phi_i$  is the observed count polar angle,  $\phi_0$  is the origin polar angle on the circle, and  $F$  is the uniform CDF.

$$U_N^2 = \min_{\text{origin on circle}, \phi_0} U_N^2(\phi_0). \quad (8)$$

Adapting a similar approach as discussed in Nurgaliev et al. (2013),  $\hat{d}_{N, C}$  is calculated in four radial annuli, which in this study they range between  $0.05R_{500}$  and  $0.5R_{500}$

#### 3.4.2. The Centroid Shift ( $w$ )

Another popular X-ray relaxation indicator is the centroid shift,  $w$ . It measures the shift of the X-ray surface brightness centroid in different radial apertures. While the intracluster medium center of mass of a system in dynamical equilibrium should scale independently, an unrelaxed system has a scale-dependent center of mass (Mohr et al. 1993). Therefore, by taking advantage of  $w$ , the relaxation status of a cluster could be determined. Centroid shift can be calculated based on the

following relation (Böhringer et al. 2010):

$$w = \left[ \frac{1}{N-1} \sum_i (\Delta_i - \langle \Delta \rangle)^2 \right]^{1/2} \times \frac{1}{R_{\text{max}}}. \quad (9)$$

In the above equation,  $\Delta_i$  is the offset between the X-ray peak and the centroid position within the  $i$ th aperture,  $N$  is the number of apertures, and  $R_{\text{max}}$  is the radius of the largest aperture. X-ray peak is selected to be the position of the brightest pixel, and centroids are specified from the moments of the exposure-corrected X-ray images. Nine apertures are chosen in the range of  $0.1R_{500}$  to  $0.5R_{500}$  with a  $0.05R_{500}$  step size.

## 4. Results

### 4.1. Relation between $\alpha_{z,0}$ and Different Relaxation Proxies

To compare different relaxation probes, introduced in Section 3, and investigate their pros and cons, we follow two steps. First, we fit a power law to the pairs of introduced proxies and  $\alpha_{z,0}$  (for  $z = 1, 0.5$ ), which provides us fitting parameters. Second, by evaluating Spearman's rank correlation coefficient, we quantify the degree of correlation between each pair. In the following subsections, we study the correlation between different relaxation probes and  $\alpha_{z,0}$  in more detail.

#### 4.1.1. Correlation between $\alpha_{z,0}$ and Photometric Probes

In Figure 1, we show the photometric indicators versus  $\alpha_{z,0}$ . The  $x$ -axis of all left panels is based on  $\alpha_{1,0}$ ; however, the right panels'  $x$ -axes are based on  $\alpha_{0.5,0}$ . Both the best-fit line with  $3\sigma$  confidence interval and the median of  $\Delta M_{12}$ ,  $D_{\text{offset}}$ , and  $B$  are demonstrated in each panel (from bottom to top). We have taken advantage of the bootstrap method with 10,000 random samplings with replacements to calculate these confidence intervals. Additionally, not only do all plots comprise scattered data, but also they involve the first (0.25) and third (0.75) quartiles ( $Q_1$  and  $Q_3$ ), shown by the shaded regions.

In the bottom panel, we show the correlations between  $\Delta M_{12}$  and  $\alpha_{z,0}$ , which we have quantified by means of the Spearman's correlation coefficient. Through the relation with  $\alpha_{1,0}$ , the correlation is positive with  $r_s = 0.35_{-0.09}^{+0.08}$  and  $\alpha = 0.71_{-0.22}^{+0.21}$ , in which  $r_s$  refers to Spearman's correlation coefficient and  $\alpha$  is the slope of the best-fit line. Following a similar approach for  $\alpha_{0.5,0}$ , we end up getting  $r_s = 0.36_{-0.09}^{+0.08}$ . Comparing the Pearson's coefficient of the  $\Delta M_{12} - \alpha_{0.5,0}$  and  $\Delta M_{12} - \alpha_{1,0}$  relations, we observe no significant difference between the Pearson's correlation coefficient of fast and slow growth; however, their slope and intercept differ slightly.

A test was run to investigate the range of growth histories that correspond to  $\Delta M_{12}$ . As can be seen from the bottom left panel, the values of  $\Delta M_{12}$  at  $\alpha_{1,0} = 0.3$  and  $\alpha_{1,0} = 0.5$  are  $\Delta M_{12} = 0.83$  and  $\Delta M_{12} = 1.2$ , respectively. We consider those halos with  $\Delta M_{12} < 0.83$  as unrelaxed and those with  $\Delta M_{12} > 1.2$  as relaxed. We find that 47% of relaxed halos are early formed ( $\alpha_{1,0} > 0.5$ ) and 13% are late formed ( $\alpha_{1,0} < 0.3$ ). On the other hand, 17% of unrelaxed halos are early formed and 33% are late formed. In light of this, there is a correlation between  $\alpha_{z,0}$  and  $\Delta m_{12}$  from which, in particular, a large number of early-formed and late-formed halos could be correctly labeled as relaxed and unrelaxed, respectively.

Moving on the second photometric proxy, we show a distribution of  $D_{\text{offset}}$  versus  $\alpha_{z,0}$  in the middle panel of

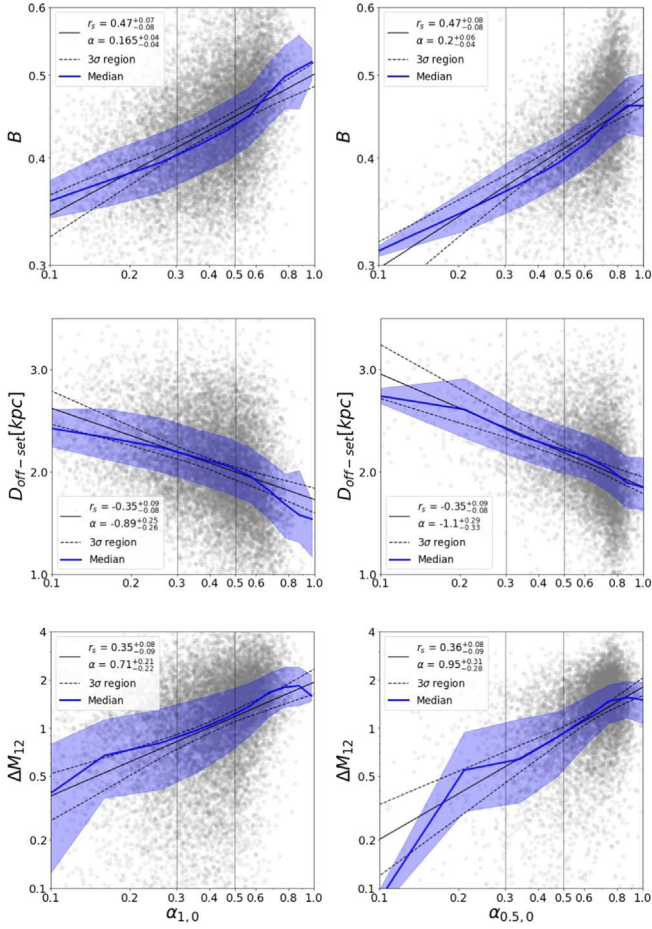


**Figure 1.** Correlation between photometric indicators ( $\Delta M_{12}$ ,  $D_{\text{offset}}$ ,  $B$ ) and the halo mass ratio at different redshifts ( $\alpha_{1,0}$ ,  $\alpha_{0,5,0}$ ). The Spearman's correlation coefficient  $r_s$  and slope are reported in each panel. Two vertical lines indicate the dynamically relaxed ( $\alpha_{1,0} > 0.5$ ) and unrelaxed groups ( $\alpha_{1,0} < 0.3$ ) (Raouf et al. 2014). The area between dashed lines is showing a  $3\sigma$  confidence interval of our fits. The first and third quartiles ( $Q_1$  and  $Q_3$ ) are illustrated in the shaded regions.

Figure 1. By studying the correlation between  $\alpha_{1,0}$  and  $D_{\text{offset}}$ , we find that the two quantities are anticorrelated with  $r_s = -0.35^{+0.09}_{-0.08}$  and  $\alpha = -0.89^{+0.25}_{-0.26}$ . Applying the same approach for  $\alpha_{0,5,0}$  brings about  $r_s = -0.35^{+0.09}_{-0.08}$ . After comparing the Pearson's coefficient of the  $D_{\text{offset}} - \alpha_{0,5,0}$  and  $D_{\text{offset}} - \alpha_{1,0}$  relations, we report no significant difference between the correlation coefficient of fast and slow growth, while their slope and intercept differ slightly.

Similar to the above investigation for luminosity gap, here we investigate the range of growth histories that correspond to  $D_{\text{offset}}$ . As can be seen in the middle left panel of Figure 1, the values of  $D_{\text{offset}}$  at  $\alpha_{1,0} = 0.3$  and  $\alpha_{1,0} = 0.5$  are  $D_{\text{offset}} = 2.17$  kpc and  $D_{\text{offset}} = 1.97$  kpc, respectively. We consider those halos with  $D_{\text{offset}} > 2.17$  kpc as unrelaxed and those with  $D_{\text{offset}} < 1.97$  kpc as relaxed. As a result, we see that 48% of relaxed halos have early formed and 11% are late formed. On the other hand, 22% of unrelaxed halos are early formed and 31% are late formed. In summary, there is an anticorrelation between  $\alpha_{z,0}$  and  $D_{\text{offset}}$  from which a large number of early-formed and late-formed halos could be correctly labeled as relaxed and unrelaxed, respectively.

Finally, in the top panels of Figure 1, after calculating the bivariate correlation for the underlying groups, we plot it as a

**Table 1**  
Correlation between  $\log(\alpha_{1,0})$  and Different Relaxation Proxies

| Proxy                     | Slope                   | Intercept               | $r_s$                   | $p$ -value |
|---------------------------|-------------------------|-------------------------|-------------------------|------------|
| $\log(A^2)$               | $-0.30^{+0.21}_{-0.24}$ | $-0.43^{+0.05}_{-0.06}$ | $-0.12^{+0.10}_{-0.09}$ | 0.01       |
| $\log(\Delta\bar{V})$     | $-0.41^{+0.08}_{-0.09}$ | $2.3^{+0.02}_{-0.02}$   | $-0.43^{+0.08}_{-0.07}$ | 0.0        |
| $\log(D_{\text{offset}})$ | $-0.89^{+0.25}_{-0.26}$ | $1.7^{+0.07}_{-0.07}$   | $-0.35^{+0.09}_{-0.08}$ | 0.0        |
| $\log(B)$                 | $0.165^{+0.04}_{-0.04}$ | $-0.3^{+0.02}_{-0.01}$  | $0.47^{+0.08}_{-0.07}$  | 0.0        |
| $\log(\Delta m_{12})$     | $0.71^{+0.21}_{-0.22}$  | $0.28^{+0.06}_{-0.06}$  | $0.35^{+0.08}_{-0.09}$  | 0.0        |

**Note**  $A^2$  and  $\Delta\bar{V}$  are spectroscopic indicators, while  $D_{\text{offset}}$ ,  $B$ , and  $\Delta m_{12}$  are photometric indicators.  $3\sigma$  confidence intervals are calculated by the bootstrap method.

**Table 2**  
Correlation between  $\log(\alpha_{0,5,0})$  and Different Relaxation Proxies

| Proxy                     | Slope                   | Intercept               | $r_s$                   | $p$ -value |
|---------------------------|-------------------------|-------------------------|-------------------------|------------|
| $\log(A^2)$               | $-0.34^{+0.26}_{-0.31}$ | $-0.43^{+0.05}_{-0.06}$ | $-0.10^{+0.09}_{-0.09}$ | 0.02       |
| $\log(\Delta\bar{V})$     | $-0.50^{+0.10}_{-0.12}$ | $2.3^{+0.02}_{-0.02}$   | $-0.42^{+0.08}_{-0.08}$ | 0.0        |
| $\log(D_{\text{offset}})$ | $-1.1^{+0.29}_{-0.33}$  | $1.85^{+0.05}_{-0.05}$  | $-0.35^{+0.09}_{-0.08}$ | 0.0        |
| $\log(B)$                 | $0.20^{+0.04}_{-0.05}$  | $-0.33^{+0.01}_{-0.01}$ | $0.47^{+0.08}_{-0.08}$  | 0.0        |
| $\log(\Delta m_{12})$     | $0.95^{+0.31}_{-0.28}$  | $0.25^{+0.04}_{-0.04}$  | $0.36^{+0.08}_{-0.09}$  | 0.0        |

**Note.**  $A^2$  and  $\Delta\bar{V}$  are spectroscopic indicators, while  $D_{\text{offset}}$ ,  $B$ , and  $\Delta m_{12}$  are photometric indicators.  $3\sigma$  confidence intervals are calculated by the bootstrap method.

function of  $\alpha_{z,0}$ . We recognize that the correlation between  $B$  and  $\alpha_{z,0}$  is significantly stronger than when we use the luminosity gap or decentering separately. The value of the Spearman's correlation coefficient,  $r_s$ , for the  $B - \alpha_{1,0}$  relation is  $0.47^{+0.08}_{-0.07}$ , and for  $B - \alpha_{0,5,0}$  turns out to be  $0.47^{+0.08}_{-0.08}$ . In addition, the best values for  $C$ ,  $D$ , and  $E$  are found to be 0.04,  $-0.11$ , and 0.28, respectively.

Same as the previous test, here we measure the range of growth histories that correspond to  $B$ . As can be seen from the top left panel of Figure 1, the values of  $B$  at  $\alpha_{1,0} = 0.3$  and  $\alpha_{1,0} = 0.5$  are  $B = 0.41$  and  $B = 0.45$ , respectively. We consider those halos with  $B < 0.41$  as unrelaxed and those with  $B > 0.45$  as relaxed. Therefore, we find that 54% of relaxed halos are early formed and 10% are late formed. Also, 16% of unrelaxed halos are early formed and 36% are late formed. As a result, a large number of early-formed and late-formed halos could be correctly labeled as relaxed and unrelaxed, respectively.

In summary, we show that the bivariate correlation, which is estimated by a combination of photometric indicators, is better than the luminosity gap or decentering with a factor of 1.3. In addition, our analysis and results are independent of the dynamical age definition ( $\alpha_{1,0}$  or  $\alpha_{0,5,0}$ ) as reported in Tables 1 and 2.

#### 4.1.2. Correlation between $\alpha_{z,0}$ and Spectroscopic Probes

In Figure 2, we show the distribution of spectroscopic indicators as a function of  $\alpha_{z,0}$ . Similar to Figure 1, the  $x$ -axis of all left panels are  $\alpha_{1,0}$  and the right panels'  $x$ -axes are  $\alpha_{0,5,0}$ . The solid straight line is the best-fit line with a  $3\sigma$  confidence interval, and the blue curves are the median of  $A^2$  and  $\Delta\bar{V}$ . All panels comprise both scattered data and also the first (0.25) and third (0.75) quartiles ( $Q_1$  and  $Q_3$ ), shown in the shaded regions.

In the top panels of Figure 2, we show the distribution of  $A^2$  versus  $\alpha_{z,0}$  using our own mock catalog explained in

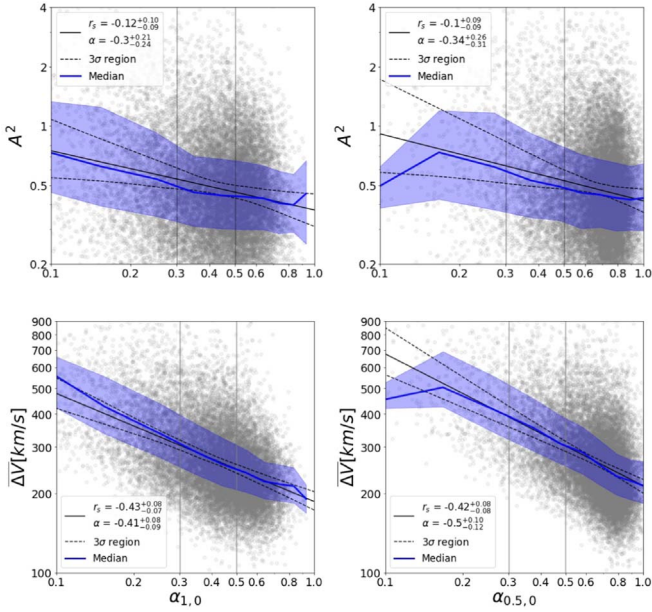


**Figure 2.** Correlation between spectroscopic indicators ( $A^2$ ,  $\Delta\bar{V}$ ) and the halo mass ratio at different redshifts ( $\alpha_{1,0}$ ,  $\alpha_{0,5,0}$ ). The Spearman's correlation coefficient  $r_s$  and slope are reported in each panel. Two vertical lines indicate the dynamically relaxed ( $\alpha_{1,0} > 0.5$ ) and unrelaxed groups ( $\alpha_{1,0} < 0.3$ ) (Raouf et al. 2014). The area between the dashed lines is showing a  $3\sigma$  confidence interval of our fits. The first and third quartiles ( $Q_1$  and  $Q_3$ ) are illustrated in the shaded regions.

Section 2.2. The Spearman's correlation coefficient for  $A^2 - \alpha_{1,0}$  is  $r_s = -0.12_{-0.09}^{+0.10}$ , and it is more or less similar to the correlation with  $\alpha_{0,5,0}$  with  $r_s = -0.10_{-0.09}^{+0.09}$ . We see from top left panel of Figure 2 that values of  $A^2$  at  $\alpha_{1,0} = 0.3$  and  $\alpha_{1,0} = 0.5$  are 0.53 and 0.46, respectively. We consider those halos with  $A^2 > 0.53$  as unrelaxed/nonvirialized and those with  $A^2 < 0.46$  as relaxed/virialized systems. Based on our calculations, 39% of virialized halos are early formed and 15% are late formed. Also, 33% of nonvirialized halos are early formed and 23% of them are late formed. Moreover, although our results suggest that there is an anticorrelation between  $\alpha_{z,0}$  and  $A^2$ , this anticorrelation is so weak that it cannot properly determine the relaxation status of galaxy systems, and using  $A^2$  cannot bring about promising results in determining whether halos are relaxed or unrelaxed in our simulation study.

In the bottom panel of Figure 2 we show the distribution of velocity segregation as a function of  $\alpha_{z,0}$  to see the correlation between these two quantities. We demonstrate that the velocity segregation is linked to the  $\alpha_{1,0}$  with  $r_s = -0.43_{-0.09}^{+0.08}$  and  $\alpha = -0.41_{-0.09}^{+0.08}$ . The Pearson correlation coefficient for  $\alpha_{0,5,0}$  turned out to be  $r_s = -0.42_{-0.08}^{+0.08}$  in a similar way. In the bottom panel of Figure 2 we reveal that the velocity segregation of the dynamically relaxed groups is smaller than the velocity segregation of unrelaxed groups, confirming the observational study of Raouf et al. (2019).

Finally, like the former arguments, we measure the range of growth histories that correspond to the velocity segregation here. From the bottom left panel, the values of  $\Delta\bar{V}$  at  $\alpha_{1,0} = 0.3$  and  $\alpha_{1,0} = 0.5$  are  $\Delta\bar{V} = 253 \text{ km s}^{-1}$  and  $\Delta\bar{V} = 208 \text{ km s}^{-1}$ , respectively. Like before, we consider those halos with  $\Delta\bar{V} > 253 \text{ km s}^{-1}$  as unrelaxed and those with  $\Delta\bar{V} < 208 \text{ km s}^{-1}$  as relaxed. Consequently, 47% of relaxed halos turn out to be early formed and 10% are late formed. On the other hand, 19% of unrelaxed halos tend to be early formed

**Table 3**  
Correlation between Different Relaxation Proxies and  $\log(\alpha_{1,0})$

| Proxy                     | Slope                   | Intercept               | $r_s$                   | $p$ -value |
|---------------------------|-------------------------|-------------------------|-------------------------|------------|
| $\log(A^2)$               | $-0.08_{-0.03}^{+0.02}$ | $-0.41_{-0.06}^{+0.05}$ | $-0.12_{-0.09}^{+0.09}$ | 0.01       |
| $\log(\Delta\bar{V})$     | $-0.50_{-0.13}^{+0.13}$ | $0.80_{-0.33}^{+0.33}$  | $-0.39_{-0.07}^{+0.07}$ | 0.0        |
| $\log(D_{\text{offset}})$ | $-0.12_{-0.07}^{+0.08}$ | $-0.17_{-0.04}^{+0.04}$ | $-0.35_{-0.08}^{+0.09}$ | 0.0        |
| $\log(B)$                 | $0.95_{-0.4}^{+0.5}$    | $-0.07_{-0.03}^{+0.05}$ | $0.47_{-0.07}^{+0.08}$  | 0.0        |
| $\log(\Delta m_{12})$     | $0.13_{-0.04}^{+0.05}$  | $-0.39_{-0.02}^{+0.01}$ | $0.35_{-0.08}^{+0.08}$  | 0.0        |

**Note.** Unlike Table 1, here we consider  $\log(\alpha_{1,0})$  as a dependent variable and various proxies as independent variables.

and 39% late formed. So, by using the velocity segregation, a large number of early-formed and late-formed halos could be correctly labeled as relaxed and unrelaxed, respectively.

In summary, when it comes to considering simulated data, we see that  $\Delta\bar{V}$  provides a strong correlation with  $\alpha_{z,0}$  compared to  $A^2$ . Moreover, we do not detect any dramatic distinction between using  $\alpha_{1,0}$  or  $\alpha_{0,5,0}$ . For a better comparison between various age indicators discussed in this section, and more details of fitting parameters and correlation coefficients, we refer the reader to Tables 1 and 2. As can be seen from the right panels of Figures 1 and 2, the majority of data is distributed in the region where  $\alpha_{0,5,0} > 0.6$ ; as a result, the slope of the best-fit line might be affected by the minority halos located at  $\alpha_{0,5,0} < 0.3$ . This is not the case for the left panels as the data are more uniformly distributed in these plots, which are based on  $\alpha_{1,0}$ .

It is worth mentioning that in all the above subsections, our null hypothesis is that there is no correlation between two variables,  $H_0 : r_s = 0$ , and our alternative hypothesis is the other way around (i.e.,  $H_1 : r_s \neq 0$ ). Since the  $p$ -value for all cases is less than 0.05, we reject the null hypothesis with a significance level of 0.05. Additionally, as we are investigating the strength of the correlation, which is quantified by means of  $r_s$ , it does not differ to consider the above relaxation probes as a function of age or the other way around. In other words, even if we consider age as a function of the relaxation probes, there will not be any difference in our results since  $r_s$  does not depend on the definition of the dependent and independent variable; however, the slope and intercept clearly change (see Table 3). The reported coefficients in Table 3 can be used to predict the age of a halo by means of the observable quantities.

#### 4.2. Relation between X-Ray and Optical Indicators

We continue our analysis by examining the relationship between the X-ray and the optical indicators. Moving on to the photometric branch, we calculate  $\Delta M_{12}$ ,  $D_{\text{offset}}$ , and  $B$  within the half virial radius for galaxy groups in the Yang catalog (Yang et al. 2005, 2007). Also, when it comes to considering the spectroscopic probes, we calculate  $A^2$  and  $\Delta\bar{V}$  for this galaxy systems. We also compute the correlation between these quantities and the X-ray proxies in a similar way used in the simulation data.

##### 4.2.1. Correlation of the X-Ray Indicators with Photometric Ones

In Figure 3 we show the distribution of the X-ray indicators, which are discussed in Section 3.4, versus three different photometric probes. The y-axis of all top panels is in terms of the photon asymmetry,  $A_{\text{phot}}$ ; however, the bottom panel's y-axis is based on the centroid shift,  $w$ . The solid straight line is

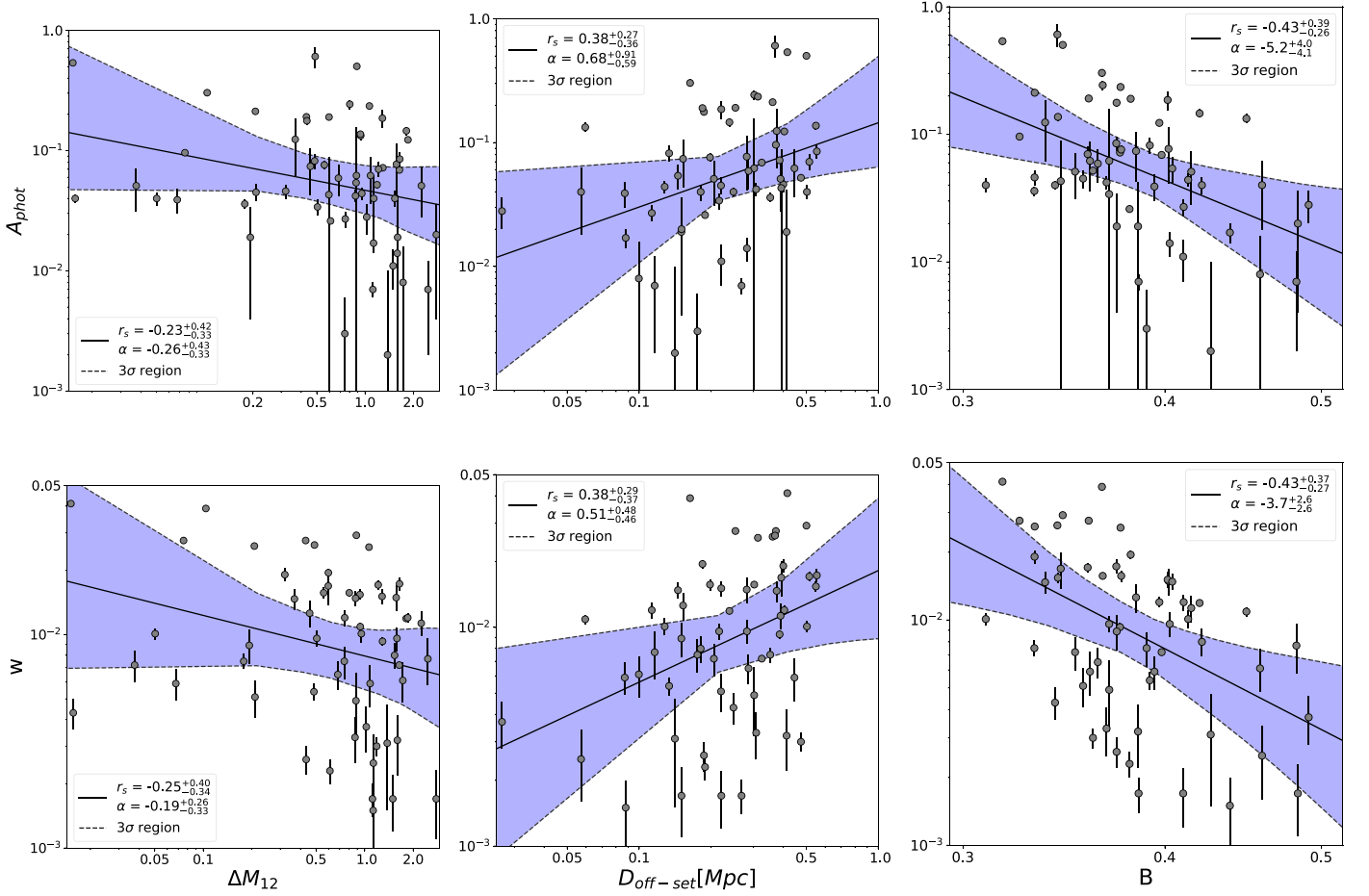


**Figure 3.** X-ray probes vs. photometric ( $\Delta M_{12}$ ,  $D_{\text{offset}}$ ,  $B$ ) relaxation indicators. The solid line is the best-fit power-law relationship. The Spearman correlation coefficient,  $r_s$ , and the best-fit power-law slope are indicated in each panel. The shaded area is showing a  $3\sigma$  confidence interval of the fits.

the best-fit line with a  $3\sigma$  confidence interval illustrated in the shaded region. All plots comprise observed data points with their error bars. For the sake of a simple comparison with results of Roberts et al. (2018), in our figures we follow a similar plotting style.

In the top left panel of Figure 3 we show the distribution of  $A_{\text{phot}}$  with measurement errors versus  $\Delta M_{12}$ . As can be seen, there is an anticorrelation with the coefficient of  $r_s = -0.24^{+0.42}_{-0.33}$ . It means that relaxed galaxy systems, which have smaller photon asymmetry, have larger  $\Delta M_{12}$ . In other words, this trend shows that by increasing  $\Delta M_{12}$ ,  $A_{\text{phot}}$  decreases. In the top middle panel we show  $A_{\text{phot}}$  versus  $D_{\text{offset}}$ , which demonstrates a correlation with the coefficient of  $r_s = 0.38^{+0.27}_{-0.36}$ . It shows that for unrelaxed systems where  $A_{\text{phot}}$  is large, the  $D_{\text{offset}}$  is large.

Moving on our second X-ray indicator, in the bottom left panel of Figure 3 we show the distribution of  $w$  with the measurement errors as a function of  $\Delta M_{12}$ . As can be seen there is anticorrelation with a coefficient of  $r_s = -0.25^{+0.40}_{-0.34}$ . It shows that relaxed groups/clusters, which have a small centroid shift, have larger  $\Delta M_{12}$ . In the bottom middle panel we show the same figure for  $D_{\text{offset}}$ , which demonstrates a correlation with  $r_s = 0.38^{+0.29}_{-0.37}$ . Therefore, we can conclude that the more a galaxy system is relaxed, the smaller  $D_{\text{offset}}$  and  $w$  should be.

Finally, in the top right panel of Figure 3 we plot  $A_{\text{phot}}$  versus  $B$ , defined in Section 3.2.3, which as a photometric indicator

shows the strongest correlation of  $A_{\text{phot}}$  with  $r_s = 0.43^{+0.27}_{-0.38}$ . It shed some light on this fact that unrelaxed systems have larger  $B$ . Also, in the bottom right panel, we show the relation between  $w$  and  $B$ . We find that this photometric indicator shows the strongest correlation of  $w$  with  $r_s = 0.43^{+0.28}_{-0.35}$ . Consequently, it can be inferred that unrelaxed systems have larger  $B$ .

In summary, an interesting aspect of these results is that the bivariate correlation,  $B = 0.04 \times \Delta m_{12} - 0.11 \times \text{Log}(D_{\text{offset}}) + 0.28$ , is a prediction rather than a relation. In other words, this photometric probe of halo relaxation shows a strong correlation with the X-ray probes with a factor of 1.8 compared to  $\Delta M_{12}$  and with a factor of 1.13 compared to  $D_{\text{offset}}$ , so it offers an economical replacement to expensive and relatively rare X-ray and spectroscopic proxies.

#### 4.2.2. Correlation of the X-Ray Indicators with Spectroscopic Ones

In Figure 4 we illustrate the X-ray indicators versus spectroscopic probes. The y-axis of all top panels are in terms of  $A_{\text{phot}}$ ; however, the bottom panels' y-axes are based on  $w$ . The solid straight line is the best-fit line with a  $3\sigma$  confidence interval is illustrated in the shaded region. All plots comprise observed data points with their error bars.

In the top left panel of Figure 4, we plot  $A_{\text{phot}}$  with the measurement errors versus  $A^2$ . As can be seen there is a correlation with the coefficient of  $r_s = 0.43^{+0.31}_{-0.38}$ . It is

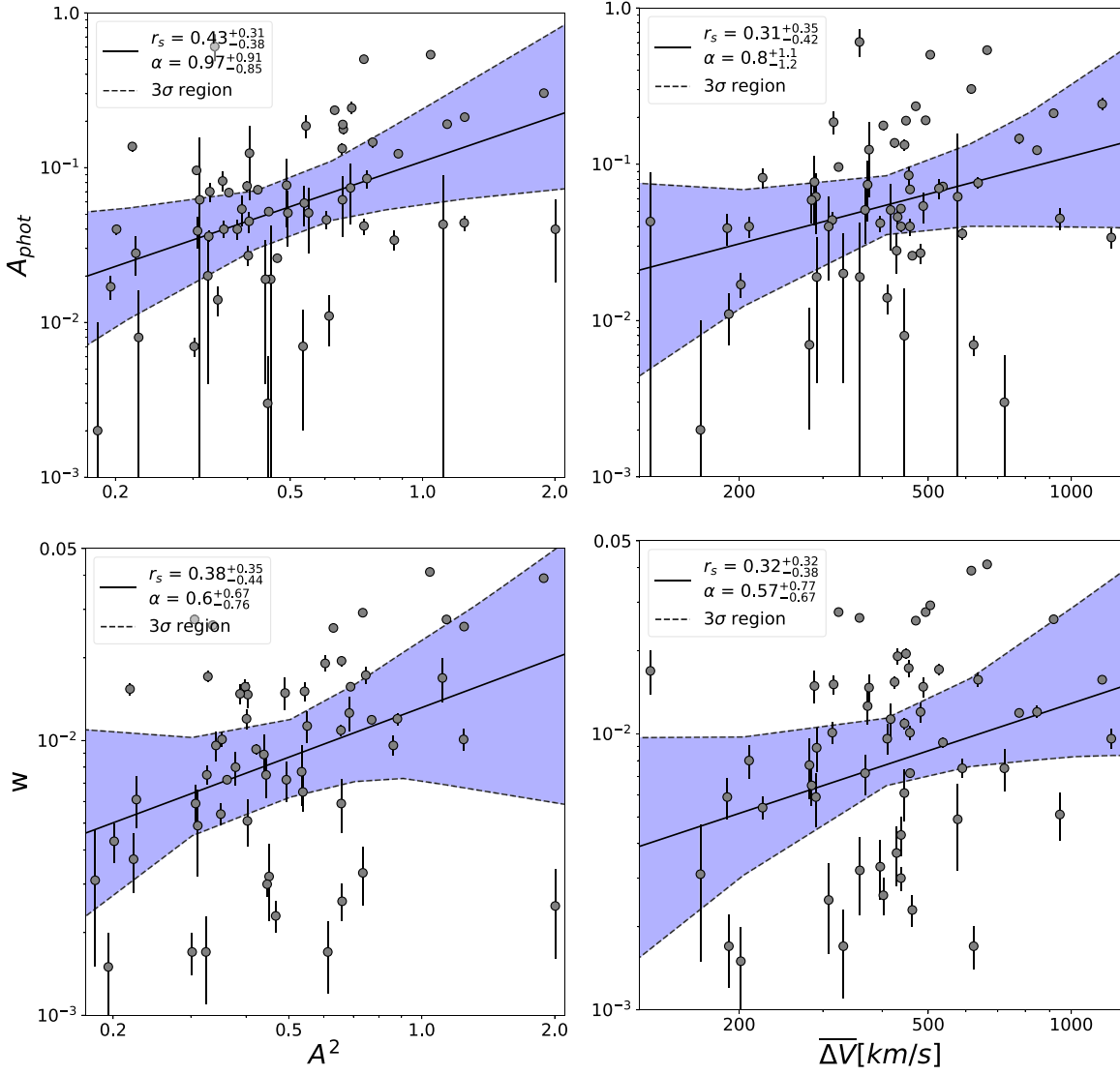


**Figure 4.** X-ray probes vs. spectroscopic ( $A^2$ ,  $\Delta\bar{V}$ ) relaxation indicators. The solid line is the best-fit power-law relationship. The Spearman correlation coefficient,  $r_s$ , and the best-fit power-law slope are indicated in each panel. The shaded area is showing a  $3\sigma$  confidence interval of the fits.

consistent with our intuition that the velocity distribution of relaxed galaxy systems is supposed to be more normal than their unrelaxed counterparts. After that, in the top right panel we plot  $A_{\text{phot}}$  versus  $\Delta\bar{V}$ , which demonstrates a correlation with the coefficient of  $r_s = 0.31^{+0.35}_{-0.42}$ .

In the bottom left panel of Figure 4 we show distribution of  $w$  with the measurement errors versus  $A^2$ . As can be seen the correlation is positive with  $r_s = 0.38^{+0.35}_{-0.44}$ . In the bottom right panel we plot  $w$  versus  $\Delta\bar{V}$ , which demonstrates a correlation with  $r_s = 0.32^{+0.32}_{-0.38}$ . As a result, apparently, relaxed systems show a small velocity segregation while unrelaxed ones show a larger segregation.

In summary, while there is a considerable correlation between AD test and the X-ray indicators, there is no significant correlation between AD test and halo mass assembly at different redshifts (see Tables 1 and 2). Furthermore, comparing the results of this section with what we find for simulated data in Section 4.1.2, we can infer that the velocity segregation has a stronger correlation with the mass assembly history at different redshifts than with X-ray indicators with a factor of  $\sim 1.34$ .

**Table 4**  
Correlation between  $\log(A_{\text{phot}})$  and Different Relaxation Proxies

| Proxy                     | Slope                   | Intercept               | $r_s$                   | $p$ -value |
|---------------------------|-------------------------|-------------------------|-------------------------|------------|
| $\log(A^2)$               | $0.98^{+0.91}_{-0.85}$  | $-0.96^{+0.32}_{-0.30}$ | $0.43^{+0.31}_{-0.38}$  | 0.001      |
| $\log(\Delta\bar{V})$     | $0.80^{+1.1}_{-1.2}$    | $-3.3^{+2.9}_{-2.9}$    | $0.31^{+0.35}_{-0.42}$  | 0.02       |
| $\log(D_{\text{offset}})$ | $0.68^{+0.91}_{-0.59}$  | $-0.83^{+0.53}_{-0.39}$ | $0.38^{+0.27}_{-0.36}$  | 0.05       |
| $\log(B)$                 | $-5.2^{+4.2}_{-3.8}$    | $3.4^{+1.6}_{-1.8}$     | $-0.43^{+0.27}_{-0.38}$ | 0.001      |
| $\log(\Delta m_{12})$     | $-0.26^{+0.43}_{-0.33}$ | $-1.3^{+0.21}_{-0.22}$  | $-0.24^{+0.42}_{-0.33}$ | 0.01       |

**Note.**  $A^2$  and  $\Delta\bar{V}$  are spectroscopic indicators, while  $D_{\text{offset}}$ ,  $B$ , and  $\Delta m_{12}$  are photometric indicators.  $3\sigma$  confidence intervals are calculated by the bootstrap method.

We would like to draw the reader's attention to the matter where the null hypothesis is rejected with a significance level of 0.05 in all of the above correlations with X-ray indicators. This is because the  $p$ -values of all the above cases are either equal or less than 0.05. All fitting parameters along with correlation parameters are provided in Tables 4 and 5.



**Table 5**  
Correlation between  $\log(w)$  and Different Relaxation Proxies

| Proxy                     | Slope                   | Intercept              | $r_s$                   | $p$ -value |
|---------------------------|-------------------------|------------------------|-------------------------|------------|
| $\log(A^2)$               | $0.60_{-0.76}^{+0.67}$  | $-1.9_{-0.27}^{+0.23}$ | $0.38_{-0.44}^{+0.35}$  | 0.02       |
| $\log(\Delta V)$          | $0.53_{-0.67}^{+0.77}$  | $-3.6_{-2.0}^{+1.7}$   | $0.32_{-0.38}^{+0.32}$  | 0.05       |
| $\log(D_{\text{offset}})$ | $0.50_{-0.46}^{+0.48}$  | $-1.7_{-0.32}^{+0.32}$ | $0.38_{-0.37}^{+0.29}$  | 0.004      |
| $\log(B)$                 | $-3.7_{-2.6}^{+2.6}$    | $3.6_{-1.1}^{+0.1}$    | $-0.43_{-0.35}^{+0.28}$ | 0.003      |
| $\log(\Delta m_{12})$     | $-0.19_{-0.33}^{+0.26}$ | $-2.1_{-0.15}^{+0.15}$ | $-0.25_{-0.34}^{+0.40}$ | 0.05       |

**Note.**  $A^2$  and  $\Delta V$  are spectroscopic indicators, while  $D_{\text{offset}}$ , B, and  $\Delta m_{12}$  are photometric indicators.  $3\sigma$  confidence intervals are calculated by the bootstrap method.

## 5. Summary and Discussion

We use the Radio–SAGE galaxy formation model to study optical and spectroscopic relaxation proxies in galaxy groups and clusters. We propose a bivariate correlation between the luminosity gap and BGG offset, built entirely on photometric indicators, which demonstrates a strong correlation with the dynamical age of galaxy groups. To have fair comparison with observations, we have made a mock catalog for our simulation catalog. In the mock catalog we compute the line-of-sight velocity that is necessary for the calculation of velocity segregation and AD statistics,  $A^2$ . For comparison, we use a sample of observational data to probe the reliability of the proposed bivariate relation in identifying the dynamically relaxed groups. Our findings can be summarized as follows:

1. We show that a combination of  $D_{\text{offset}}$  and  $\Delta m_{12}$  as a new photometric indicator, bring about a strong Pearson’s correlation coefficient with the dynamical age. After fitting the simulated data, we find the bivariate benchmark as a function of the luminosity gap and decentering ( $B = 0.04 \times \Delta m_{12} - 0.11 \times \text{Log}(D_{\text{off-set}}) + 0.28$ ). This relation demonstrates a stronger correlation with  $\alpha_{z,0}$  compared to just using the luminosity gap or centroid shift individually.
2. From simulations, we show that the bivariate benchmark is more desirable than the AD test. This is because the correlation between mass assembly and bivariate correlation is much stronger than the correlation between the AD test and mass assembly by a factor of  $\sim 3.6$ . We also show that by considering those halos with  $B < 0.41$  as unrelaxed and those with  $B > 0.45$  as relaxed, 54% of relaxed halos are early formed and 10% late formed. Also, 16% of unrelaxed halos are early formed and 36% are late formed.
3. From our fittings, we see that using either  $\alpha_{1,0}$  or  $\alpha_{0.5,0}$  leads to slightly different slopes and intercepts. However, we observe no significant difference in the Pearson’s correlation coefficients of these two cases. Therefore, we show that considering fast or slow growth does not have any impact on our analysis. Also, as the slopes of the best-fit lines associated with  $\alpha_{0.5,0}$  are steeper than their counterpart, it can be inferred that they are more sensitive to the changes of the halo mass assembly.
4. Using the observational data we show that a combination of  $D_{\text{offset}}$  and  $\Delta m_{12}$ , which we define as the bivariate correlation, considerably improves the strength of the correlation coefficient between this indicator and the X-ray proxies like photon asymmetry and centroid shift. Compared to using the luminosity gap or decentering

individually, this new probe leads to stronger correlations.


5. From observations, through the velocity segregation, there is a stronger correlation between bivariate benchmark and X-ray proxies. Also, when it comes to considering the correlation between AD statistics and X-ray probes, we notice that AD statistics leads to the same value as the one between the bivariate benchmark and photon asymmetry. However, the correlation between the AD statistics and centroid shift is weaker than the correlation between the bivariate benchmark and centroid shift.

Through the analysis on simulations data, considering the AD statistics, the velocity segregation has a stronger correlation with the halo mass assembly. In contrast, observational data show that AD statistics has a stronger correlation with the X-ray indicators than the velocity segregation. Furthermore, we show that while the AD statistics appears to be a good indicator for halo relaxation for the observed data, it is not a highly distinctive probe when applied to simulated data. One possible explanation is that there is no spatial X-ray information in the simulations to make a direct comparison with the observations. Therefore, we rely on indirect halo relaxation indicators. The halo age in simulations is based on the dark matter, while in the observations it is based on the baryonic component. Another factor that plays a role is that all the halo virialization/relaxation indicators, photometric, spectroscopic, and X-rays, have drawbacks due to the projection effects. However, they are statistically useful methods for estimation of the dynamical age. Also, as the uncertainties in the data are quite large, simply fitting a linear line cannot describe the real variation of the data; however, we add the linear regression to emphasize the general trend of the data.

This study suggests that the photometric relaxation proxies are as well as, if not better than, their spectroscopic counterparts. We support this claim through investigating simulated data as well as observational data. Given the challenges of spectroscopic observations, the photometric data will work as well when it comes to quantifying the halo age. Consequently, it appears to be both economical and reliable to use the bivariate correlation B to attribute relaxation to galaxy systems.

We thank Ian Roberts for providing us with the X-ray data used in Roberts et al. (2018). His help has undoubtedly allowed this analysis to progress faster.

## ORCID iDs

Mohammad H. Zhooldideh Haghighi  <https://orcid.org/0000-0001-5759-0302>

Mojtaba Raouf  <https://orcid.org/0000-0002-1496-3591>

Amin Farhang  <https://orcid.org/0000-0001-7712-697X>

## References

- Barnes, J. E. 1989, *Natur*, **338**, 123
- Blaizot, J., Wadadekar, Y., Guiderdoni, B., et al. 2005, *MNRAS*, **360**, 159
- Böhringer, H., Pratt, G. W., Arnaud, M., et al. 2010, *A&A*, **514**, A32
- Carollo, C. M., Cibinel, A., Lilly, S. J., et al. 2013, *ApJ*, **776**, 71
- Dariush, A., Khosroshahi, H. G., Ponman, T. J., et al. 2007, *MNRAS*, **382**, 433
- Dariush, A. A., Raychaudhury, S., Ponman, T. J., et al. 2010, *MNRAS*, **405**, 1873
- Dark Energy Survey Collaboration, Abbott, T., Abdalla, F. B., et al. 2016, *MNRAS*, **460**, 1270

- Davis, M., Efstathiou, G., Frenk, C. S., et al. 1985, *ApJ*, 292, 371
- Davis, M., Efstathiou, G., Frenk, C. S., & White, S. D. M. 1985, *ApJ*, 292, 371
- Dietrich, J. P., Böhnert, A., Lombardi, M., Hilbert, S., & Hartlap, J. 2012, *MNRAS*, 419, 3547
- D’Onghia, E., Sommer-Larsen, J., Romeo, A. D., et al. 2005, *ApJL*, 630, L109
- Duarte, M., & Mamon, G. A. 2015, *MNRAS*, 453, 3848
- Eke, V. R., Baugh, C. M., Cole, S., et al. 2005, *MNRAS*, 362, 1233
- Ellison, S. L., Patton, D. R., Simard, L., & McConnell, A. W. 2008, *AJ*, 135, 1877
- Farhang, A., Khosroshahi, H. G., Mamon, G. A., et al. 2017, *ApJ*, 840, 58
- Gozaliasl, G., Finoguenov, A., Tanaka, M., et al. 2019, *MNRAS*, 483, 3545
- Gozaliasl, G., Khosroshahi, H. G., Dariush, A. A., et al. 2014, *A&A*, 571, A49
- Hashimoto, Y., Oemler, A., Lin, H., et al. 1998, *ApJ*, 499, 589
- Horellou, C., Intema, H. T., Smolčić, V., et al. 2018, *A&A*, 620, A19
- Hou, A., Parker, L. C., Balogh, M. L., et al. 2013, *MNRAS*, 435, 1715
- Hou, A., Parker, L. C., Harris, W. E., & Wilman, D. J. 2009, *ApJ*, 702, 1199
- Huchra, J. P., & Geller, M. J. 1982, *ApJ*, 257, 423
- Jones, L. R., Ponman, T. J., Horton, A., et al. 2003, *MNRAS*, 343, 627
- Khosroshahi, H. G., Jones, L. R., & Ponman, T. J. 2004, *MNRAS*, 349, 1240
- Khosroshahi, H. G., Maughan, B. J., Ponman, T. J., & Jones, L. R. 2006, *MNRAS*, 369, 1211
- Khosroshahi, H. G., Ponman, T. J., & Jones, L. R. 2006, *MNRAS*, 369, 1211
- Khosroshahi, H. G., Ponman, T. J., & Jones, L. R. 2007, *MNRAS*, 377, 595
- Khosroshahi, H. G., Raouf, M., Miraghaei, H., et al. 2017, *ApJ*, 842, 81
- Lares, M., Lambas, D. G., & Sánchez, A. G. 2004, *MNRAS*, 352, 501
- Lavoie, S., Willis, J. P., Démoclès, J., et al. 2016, *MNRAS*, 462, 4141
- McGee, S. L., Balogh, M. L., Wilman, D. J., et al. 2011, *MNRAS*, 413, 996
- Mohr, J. J., Fabricant, D. G., & Geller, M. J. 1993, *ApJ*, 413, 492
- Nascimento, R. S., Lopes, P. A. A., Ribeiro, A. L. B., et al. 2019, *MNRAS*, 483, L121
- Nurgaliev, D., McDonald, M., Benson, B. A., et al. 2013, *ApJ*, 779, 112
- Oguri, M., Takada, M., Okabe, N., & Smith, G. P. 2010, *MNRAS*, 405, 2215
- Parekh, V., van der Heyden, K., Ferrari, C., Angus, G., & Holwerda, B. 2015, *A&A*, 575, A127
- Peng, Y., Maiolino, R., & Cochrane, R. 2015, *Natur*, 521, 192
- Ponman, T. J., Allan, D. J., Jones, L. R., et al. 1994, *Natur*, 369, 462
- Press, W. H., & Davis, M. 1982, *ApJ*, 259, 449
- Raouf, M., Khosroshahi, H. G., & Dariush, A. 2016, *ApJ*, 824, 140
- Raouf, M., Khosroshahi, H. G., Mamon, G. A., et al. 2018, *ApJ*, 863, 40
- Raouf, M., Khosroshahi, H. G., Ponman, T. J., et al. 2014, *MNRAS*, 442, 1578
- Raouf, M., Shabala, S. S., Croton, D. J., Khosroshahi, H. G., & Bernyk, M. 2017, *MNRAS*, 471, 658
- Raouf, M., Silk, J., Shabala, S. S., et al. 2019, *MNRAS*, 486, 1509
- Raouf, M., Smith, R., Khosroshahi, H. G., et al. 2019, *ApJ*, 887, 264
- Ribeiro, A. L. B., de Carvalho, R. R., Trevisan, M., et al. 2013, *MNRAS*, 434, 784
- Roberts, I. D., Parker, L. C., & Hlavacek-Larrondo, J. 2018, *MNRAS*, 475, 4704
- Sanderson, A. J. R., Edge, A. C., & Smith, G. P. 2009, *MNRAS*, 398, 1698
- Skibba, R. A., van den Bosch, F. C., Yang, X., et al. 2011, *MNRAS*, 410, 417
- Smith, G. P. 2005, *MNRAS*, 359, 417
- Springel, D. J., White, V., De Lucia, S. D. M., et al. 2006, *MNRAS*, 365, 11
- Springel, V., White, S. D. M., Jenkins, A., et al. 2005, *Natur*, 435, 629
- Springel, V., White, S. D. M., Tormen, G., & Kauffmann, G. 2001, *MNRAS*, 328, 726
- Stephens, M. A. 1974, *J. Am. Stat. Assoc.*, 69, 737
- Watson, G. S. 1961, *Biometrika*, 48, 109
- Wilman, D. J., Balogh, M. L., Bower, R. G., et al. 2005, *MNRAS*, 358, 88
- Yahil, A., & Vidal, N. V. 1977, *ApJ*, 214, 347
- Yang, X., Mo, H. J., van den Bosch, F. C., et al. 2005, *MNRAS*, 356, 1293
- Yang, X., Mo, H. J., van den Bosch, F. C., et al. 2007, *ApJ*, 671, 153